Progress In Electromagnetics Research B, Vol. 67, 1–16, 2016

Categorized UWB On-Body Radio Channel Modeling for WBANs

Timo Kumpuniemi*, Matti Hämäläinen, Kamya Yekeh Yazdandoost, and Jari Iinatti

Abstract—A categorized radio channel modeling for wireless ultra-wideband on-body body area networks is discussed. Measurements in an anechoic chamber at fourteen antenna locations are conducted in a 2–8 GHz band. The dipole and double loop antenna types are used. Six link classes are formed based on the antenna spots on the torso, head or limb. The limb-limb and the head-limb links have the lowest and highest path losses, respectively. The head-limb links have the shortest channel impulse responses (CIRs) and limb-limb links the longest ones. The CIR amplitudes follow the inverse Gaussian distribution. The tap indexes and the total excess delays are modeled with the negative binomial distribution. In most cases, the CIRs decay faster for the dipole. Otherwise no major differences exist between the antennas.

1. INTRODUCTION

The size of the electronic devices is constantly decreasing giving the possibility to place them in very compact volumes. As also power consumptions are lowering they can be placed in almost everywhere, including the vicinity of a human body. The devices can be attached to the closeness of human bodies, on the body or even inside the body. The body area networks (BANs) consisting of several sensors can be divided into on-body, off-body or in-body cases depending on the location of the devices [1]. The available apparatuses aimed at the human well-being, where the user can monitor the sensor data from his own body describing, e.g., his physical activity or development of his fitness related to various sorts of activities are one result of this development. The ageing of populations in many developed countries, on the other hand, has forced to start looking for help from the technology when facing many problems resulting from this demographic development. For medical purposes, devices for monitoring a patient's vital functions and health conditions by a patient himself or a doctor have been under vivid discussion during the last decade. When the apparatuses are wireless, the patient can lead his life in his home environment or outdoors as the wireless technology enables a free mobility and a remote monitoring of his vital data by the doctor [2].

The ultra-wideband (UWB) technology is very suitable to wireless body area networks (WBANs) due to its large bandwidth. It offers a low transmission power and thus low interference and a low power consumption, a simple device structure and an excellent robustness against difficult radio channel conditions [3]. As the international standard IEEE 802.15.6 [4] was published in 2012, it contained the UWB as a mandatory physical layer technique for the BANs. It has been investigated both in off-body [5–7] and in-body cases [8]. Perhaps the majority of the published papers are related to the various aspects of on-body situations [9–12]. For instance, in [7, 13–15] research related to UWB on-body radio channels are reported. In [7, 12, 16–19], the effect of different antennas or polarizations on the UWB links are investigated. References [20, 21] contain examination of body shapes and postures on the UWB on-body communications and in [22] the energy absorption of the UWB signal by the human body is found out.

Received 31 December 2015, Accepted 26 March 2016, Scheduled 4 April 2016

* Corresponding author: Timo Kumpuniemi (timo.kumpuniemi@ee.oulu.fi).

The authors are with the Centre for Wireless Communications, Faculty of Information Technology and Electrical Engineering, University of Oulu, P. O. Box 4500, FI-90014 University of Oulu, Finland.

This article considers categorized UWB on-body WBAN channel models based on static frequency domain measurements across 2–8 GHz band carried out with a vector network analyzer (VNA) in an anechoic chamber. The motivation for the work is to examine the differences between radio channels around the complex environment of a human body and to produce suitable models to be used, e.g., in computer simulations. The categorization rule is different from the previously presented ones [15, 23–25] as it is based on the antenna locations on the body. The work is done with two prototype antenna types: dipole and double loop. The categorized path loss models and statistical model for the channel impulse response (CIR) amplitudes and delay spread are presented for each category. The work extends the results of a more thorough WBAN measurement and analysis initiative, whose previous results are reported, e.g., in [18, 19, 23, 26].

The structure of this article is as follows. In Section 2 the measurement setup is introduced. Section 3 explains the measurement scenario and the selection of the antenna locations. In Section 4 the data analysis and results are introduced. In Section 5 conclusions and plans for the future work are given.

2. MEASUREMENT SETUP

The measurement campaign was conducted in an anechoic chamber with floor dimensions of 2.45 m by 3.65 m and room height of 2.4 m. The chamber was installed in a 60 m^2 large electromagnetic compatibility room. A 1.83 m tall male served as the test person wearing a cotton T-shirt and jeans. The belt, shoes and all easily removable metal containing items were absent, not including jeans buttons and rivets.

The VNA in use was a four-port model ZVA8 by Rohde & Schwarz. Eight meter long measurement cables were connected to each port and lead into the chamber for attaching the antennas to the other cable ends. The VNA was set to sweep the 1601 frequency points in the 2–8 GHz band 100 times with a sweep time setting of 288.18 ms and transmit power of +10 dBm. Both forward and reverse channels were recorded resulting 12 channels for a single four-antenna instalment. Further information of the measurement setup is in [18].

The planar prototype antennas (dipole and double loop) used in the work are shown in Fig. 1 where the ruler is in centimeters. The antenna substrate material is TRF-43 by Taconic. The maximum total gains of the antennas in free space are 6 dBi and the usable frequency range is 2–12 GHz. The structures and performances of the antennas used in the work in free space and in on-body cases are described in detail in [26–28].

3. SELECTION OF ANTENNA LOCATIONS AND MEASUREMENT IMPLEMENTATION

The selection of the antenna locations on the body for the measurements was based on the existing and easily assumed positions for sensors that can be used to monitor different parameters of the human body functions. For example, [29] presents a wearable medical monitoring and alert system that is capable of measuring the blood pressure, the oxygen saturation (SpO_2), a one lead electrocardiogram (ECG) and user activity with acceleration sensors from the user's wrist. In [30] a prototype BAN is presented where several sensors are attached at the head area to be used for sleep monitoring. Several sensor locations that could be used to monitor various vital parameters are listed in [31]: the heart rate can be measured at a finger, ear, auditory canal, auricular area and forehead whereas SpO_2 level can be obtained from a sensor at a finger or forehead. ECG sensors can be integrated into, e.g., T-shirt or other clothing at different parts of the body. Ref. [32] reports the usage of accelerometers located at a patient's both wrists and the left ankle to monitor the Parkinson's disease. In [33], the same disease is monitored by using accelerometers installed at the trunk of a patient. For sports applications, [34] presents a motions tracking system based on inertial sensors placed at the hip, leg and foot.

As a result of listing the existing and possible sensor locations, fourteen spots were used for measurements as shown in Fig. 2. Three spots (1–3) lay on the head, six at the limbs (6, 7, 9, 11–13) and the rest were on the torso. The sites 4, 6, 8, 10 and 12 exist on the side of the torso, arm or leg whereas the remaining spots are situated on their frontal parts. Six combinations of four sites were

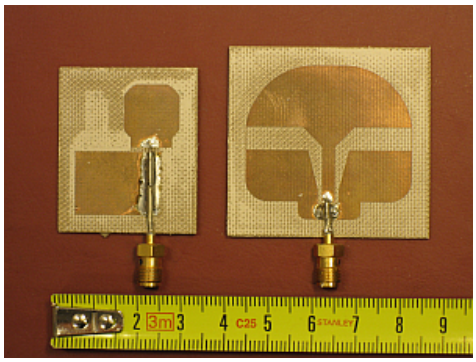

(a) (b)

Figure 1. (a) Dipole and (b) double loop antennas.

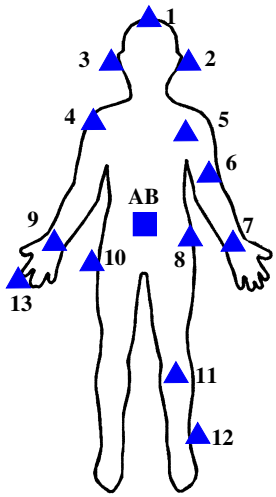

Figure 2. Antenna locations.

Table 1. Measured location combinations.

AB-1-7-9	AB-5-6-7	AB-1-2-3
AB-4-8-10	AB-4-9-13	AB-10-11-12

selected and they are collected in Table 1. As observed, in all cases the spot at the AB is included. It was located either on the abdomen, as shown in Fig. 2, or on a pole off the body. The off-body links are not covered in this article, thus these links are absent from the results. The measurements were performed for both antenna types. The antenna distance was set to 20 mm from the body surface by inserting ROHACELL material between the antenna-body gap. In [27], the 20 mm body-antenna separation was noted to produce a similar antenna matching to the free space environment. In [28], the 20 mm distance resulted an improved path loss performance compared to smaller gap thicknesses. The material has similar electrical properties as air (the relative permittivity $\epsilon_r = 1.05$ at 2.5 GHz, 1.043 at 5 GHz, 1.046 at 10 GHz). Finally, all measurements were fully repeated to average out the effect of variations in antenna placement on the body. As a result, 252 links were measured containing 25200 separate frequency sweeps.

4. DATA ANALYSIS AND RESULTS

4.1. Data Post-Processing

The recorded frequency domain data was post-processed to obtain the corresponding time-domain channel impulse response (CIR) for each channel by using the inverse fast Fourier transform (IFFT) algorithm. IFFT was applied directly to the complex raw data resulting complex CIRs as well, i.e., the complex baseband method was applied [3]. No windowing functions were used. The absolute values of the CIRs were utilized in the actual data analysis. The resulting time resolution of the CIRs is the inverse of the measurement bandwidth, i.e., $\Delta t = (1/6 \cdot 10^9) \approx 0.167$ ns. This corresponds to a distance of approx. 5 cm assuming the speed the light for the signal propagation speed.

When solving the link distance based on the arrival time of the first arriving path of the CIR, an evident error occurs due to the lowered propagation speed of the signal in the antenna structures. The velocity is lower than the speed of light due to the electrical permittivity of the antenna substrate. The VNA, on the other hand, calibrates the zero delay plane to be at the ends of the measurement cables. Adding the antennas causes an increase in distance for the signal to pass before entering into air. The antenna dimension together with the propagation velocity less than the speed of light have the effect

that the links appear to be longer than in reality. In [18] this phenomenon was noticed to cause errors in path loss models in short link distances such as WBAN links. The antennas in [18] were the same as in this paper, and therefore the noted average distance error (90 mm for the dipole, 109 mm for the double loop) are corrected from the CIRs before data analysis.

4.2. Link Categorization

Let us assume a BAN system that is used for monitoring the heart condition with a sensor at the chest for ECG, at the ear for heartbeat and at the wrist for SpO_2. The data collected from the sensors are collected to the on-body access point AB and the data is sent from AB to an off-body node located, e.g., on a wall of a room as illustrated in Fig. 3. Fig. 4 shows example CIRs for this scenario. The AB-5 is the link between the abdomen and chest, AB-3 is the abdomen-right ear link and AB-9 is the abdomen-right wrist link. It is noted from the figure, that considerable differences exist between the example CIRs. A single generic channel model is not able to describe the behavior of all links very accurately in all cases and there is a need for a more sophisticated approach to describe the link characteristics.

In [18, 19], the identical data as in this article was used to produce generic channel models for these two antennas. In this paper, the work is extended by categorizing the on-body links based on the location of the antennas on a limb, the torso, or the head. As a result six classes are obtained: torso-torso (TT), torso-head (TH), torso-limb (TL), head-limb (HL), limb-limb (LL) and head-head (HH). The propagation mechanisms of the radio wave are different in those classes. For instance, in TT and HH the wave propagates as surface or creeping waves in the vicinity of the body following its morphology, in LL mostly as free-space like waves in the air and in TL as a mixture of these two. This division gives a more detailed view of the radio channel behavior compared to a generic model containing all the

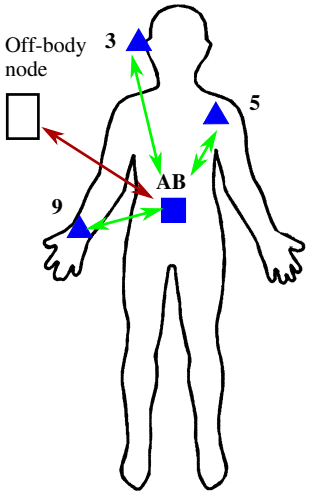

Figure 3. Example of a use case.

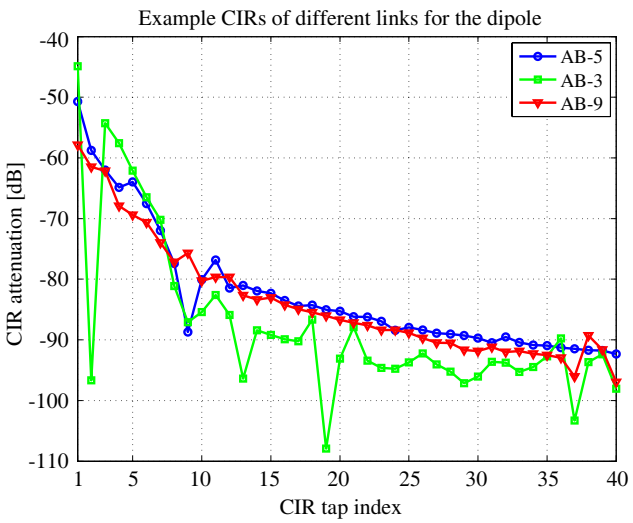

Figure 4. Example CIRs at different links.

Table 2. Channel categorization.

TT (5400)	AB-5, AB-10, AB-4, AB-8, AB-10, 4-8, 4-10, 8-10
TH (1600)	AB-1, AB-2, AB-3
TL (9200)	AB-6, AB-7, 5-6, 5-7, AB-9, AB-11, AB-12, 10-11, 10-12, AB-9, AB-13, 4-9, 4-13
HL (2000)	1-7, 1-9
LL (4000)	6-7, 7-9, 11-12, 9-13
HH (3000)	1-2, 1-3, 2-3

link types in one dataset. Furthermore, the insight is different than in other articles in the field, where the categorization for the data analysis is done usually by separating the cases of line-of-sight (LOS), non-line-of-sight (NLOS) and possibly obstructed or quasi line-of-sight (OLOS/QLOS) [15, 23–25]. The link division based on the antenna locations is objective, whereas the division based on the degree of line-of-sight conditions is always more or less subjective. The LOS/OLOS/NLOS separation is valid in many cases as long as the body posture remains constant. Considering the available combinations in Table 1 and the above-mentioned categorization, the links are sorted as shown in Table 2. The number of measured CIRs for each category for one antenna type is stated in the brackets.

4.3. Path-Loss Models

For each category, path loss (PL) models were developed by using the first order linear least squares polynomial data fitting [35]. The PLs at a distance d were modeled according to [36]

$$\mathrm{PL}(d) = \mathrm{PL}(d_0) + 10n \log_{10}\left(\frac{d}{d_0}\right) + S, \tag{1}$$

where d_0 is the reference distance 50 mm, $\mathrm{PL}(d_0)$ is the PL in dB at d_0, n is the PL exponent and S is the random scattering term. Examples of the dipole antenna with TL category and the double loop antenna with TT category are shown in Figs. 5(a) and 5(b). The blue dots show the empirical data and the data fitting to them is expressed with the red line. The numerical values of the categorized path loss models are collected in Table 3 for the both antennas separately.

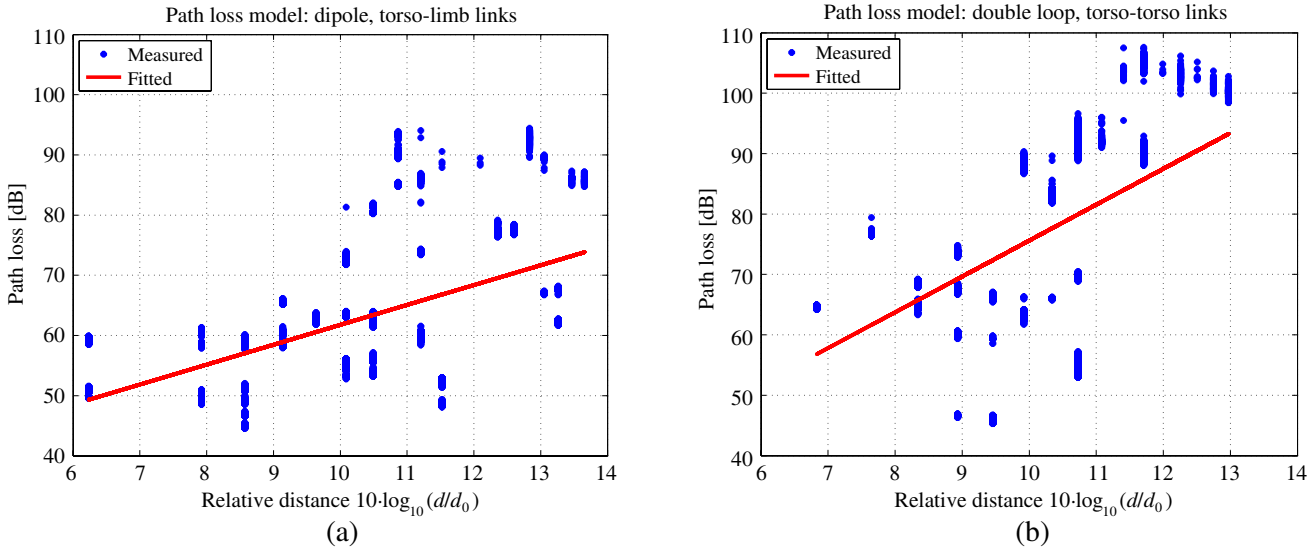

Figure 5. Examples of empirical data and their fittings. (a) Dipole with TL category. (b) Double loop with TT category.

The generic PL model in [18] based on processing all available measurement data as one set without categorization resulted $n = 3.3$ and 2.7, and $\mathrm{PL}(d_0) = 31.6$ dB and 39.8 dB for the dipole and double loop antenna, respectively. The values in Table 3 show a variation of $n = 2.5$–7.5 and $\mathrm{PL}(d_0) = -19.9$–48.1 dB in the parameters between the link classes excluding the HL case. It can therefore be deducted that the general path loss models in [18] in many cases give quite a rough view of the steepness of the signal attenuation. On the other hand, the generic models seem to be quite accurate in some of the observed link categories, e.g., TL and LL, in Table 3. In [18] it was noted that n is larger for the dipole in the generic case considering all links, but from the categorized values such a conclusion cannot be done.

The HL case gives abnormal parameter values, since according to the PL model in (1), the signal strength seems to rise as the distance increases. This has several reasons. The PL measurement geometry

Table 3. Path loss parameters.

		TT	TH	TL	HL	LL	HH
Dipole	n	4.9	7.5	3.3	−17.7	3.8	5.4
	PL(d_0)	23.2	−19.9	28.8	309.7	18.3	24.7
	σ_S, [dB]	11.7	5.1	10.6	4.6	4.6	2.2
	$\overline{X}_{\mathrm{PL}}$, [dB]	63.9	63.4	56.4	77.0	50.2	63.9
Double loop	n	5.9	5.4	3.1	−22.7	5.8	2.5
	PL(d_0)	16.2	−2.0	33.45	366.8	−2.1	48.1
	σ_S, [dB]	13.6	10.1	10.7	4.3	6.0	4.9
	$\overline{X}_{\mathrm{PL}}$, [dB]	64.4	57.2	59.7	73.3	49.7	65.3

is strongly shadowing dependent, not distance dependent. Shorter links are facing relatively stronger effects caused by shadowing than the longer ones. In an on-body BAN case, the human body blocks the signal propagation in certain directions depending on the location of the antenna [20]. The HL links are almost symmetrical in the measurements and have no major difference in the link distances. Also the number of links is limited in the observed HL category. The used antennas have radiation patterns with up to 30 dB differences in total gain depending on the direction and frequency in free space [26]. The vicinity of the human body affects the radiation patterns even further [20]. The antenna pattern effect increases the effect of the human blockage phenomenon. Therefore, it can be concluded that the classical path loss model does not always describe properly the behavior of such links where the shadowing is the dominating path loss source and the differences in link distances are narrow. The model in short link lengths, as body area networks, should be a function of shadowing degree instead of the distance but the degree of the shadowing for a link is a difficult task to solve objectively. The possible unsuitability of the classical path loss model (1) for BANs is discussed also in [37].

The standard deviation σ_S is calculated from the decibel values after normalizing the measured values around the x-axis. This was done by calculating the first order linear model values calculated with PL(d_0) and n and subtracting them from the measured values, i.e., the red line in Figs. 5(a) and 5(b) was subtracted from the blue dots describing the empirical data. σ_S gives a measure for the homogeneity of the links. In TT and TL, the links are most dissimilar, since σ_S has the largest values varying between 10.6–13.6 dB. Finally, in order to give a general view of the goodness of the links, the average path loss value $\overline{X}_{\mathrm{PL}}$ of the first arriving signal path is stated. The results vary between $\overline{X}_{\mathrm{PL}} = 49.7$–$77.0$ dB. Based on $\overline{X}_{\mathrm{PL}}$, the best link type is the LL since the path loss is the smallest at the level of 50 dB whereas the HL links attenuate the transmitted signal most, approx. 75 dB. However, it should be noted that the antenna locations are at the most mobile spots of the body in the LL links. If the use scenario is a dynamic one, the LL links most probably will face greater change than other link categories in channel conditions compared to the static one presented in Table 3.

The distribution of S was solved by fitting the data to beta (A), Birnbaum-Saunders (B), exponential (C), extreme value (D), gamma (E), generalized extreme value (F), generalized Pareto (G), inverse Gaussian (H), logistic (I), log-logistic (J), log-normal (K), Nakagami (L), normal (M), Rayleigh (N), Rician (O), t location-scale (P) and Weibull (Q) distributions. The data was normalized similarly as described in the previous paragraph when extracting the σ_S. The second order Akaike information criterion (AICc) was used as the ranking method for the distributions. The AICc is defined by the equation [38]

$$\mathrm{AICc} = -2\log\left(\mathcal{L}(\hat{\theta})\right) + 2K\left(\frac{n}{n-K-1}\right), \tag{2}$$

where $\mathcal{L}(\hat{\theta})$ is the likelihood function of the estimated parameters $\hat{\theta}$, $\log(\cdot)$ the natural logarithm, n the sample size and K the number of estimable parameters in a distribution. The AICc difference of a distribution is stated as [38]

$$\Delta_i = \mathrm{AICc}_i - \mathrm{AICc}_{\min}, \tag{3}$$

where $\mathrm{AICc}_{\min}$ is the smallest observed AICc value and AICc_i the AICc value of the ith distribution. In [38] it is stated that for large data sample sizes, i.e., the sample size $N > 10\,\mathrm{K}$, values $\Delta_i \geq 0$ indicate the model be poor in approximating the data. The distribution with the lowest AICc value was selected to be the best model, i.e., the distribution having $\Delta_i = 0$. Another metrics often reported [13] in conjunction with AICc and Δ_i is the Akaike weight defined as [38]

$$w_i = \frac{\exp\left(-\frac{1}{2}\Delta_i\right)}{\sum_{s=1}^{R}\exp\left(-\frac{1}{2}\Delta_s\right)}, \tag{4}$$

where R is the number of models. The Akaike weight can be understood to describe the probability of a distribution to be the best model among the set of R distributions.

Fitting was successful for six distributions. The values of AICc differences and Akaike weights are collected in Table 4 for all fits. The best model is on the leftmost column and the poorer fits are listed in ascending order ending up to the weakest model on the rightmost column. The generalized extreme value distribution (F) was the best fit in four cases, the generalized Pareto (G) distribution in eight cases. The Δ_i has high values leaving no doubt that the selected distribution would not be the best one. This is noted also in the w_i values that give a probability of one that a correct model has been selected.

Table 4. AICc differences and Akaike weights for path loss statistical models.

		Dipole						Double Loop					
TT	Dist.	G	F	M	P	I	D	G	F	D	M	P	I
	Δ_i	0	417	498	501	674	1120	0	26	164	1113	1115	1346
	w_i	1.0	0.0	0.0	0.0	0.0	0.0	1.0	0.0	0.0	0.0	0.0	0.0
TH	Dist.	G	F	M	P	I	D	G	F	M	P	D	I
	Δ_i	0	249	309	310	414	588	0	718	793	795	911	965
	w_i	1.0	0.0	0.0	0.0	0.0	0.0	1.0	0.0	0.0	0.0	0.0	0.0
TL	Dist.	F	G	M	P	I	D	G	F	M	P	I	D
	Δ_i	0	83	511	513	752	2929	0	2556	3760	3761	4455	5717
	w_i	1.0	0.0	0.0	0.0	0.0	0.0	1.0	0.0	0.0	0.0	0.0	0.0
HL	Dist.	F	M	D	P	I	G	F	D	G	M	P	I
	Δ_i	0	230	232	232	442	799	0	94	120	311	313	395
	w_i	1.0	0.0	0.0	0.0	0.0	0.0	1.0	0.0	0.0	0.0	0.0	0.0
LL	Dist.	G	F	D	M	P	I	F	M	P	G	I	D
	Δ_i	0	756	1327	1951	1953	2145	0	119	121	309	346	984
	w_i	1.0	0.0	0.0	0.0	0.0	0.0	1.0	0.0	0.0	0.0	0.0	0.0
HH	Dist.	G	F	M	P	I	D	G	F	D	M	P	I
	Δ_i	0	1161	1286	1288	1587	1608	0	697	1751	2496	2498	2712
	w_i	1.0	0.0	0.0	0.0	0.0	0.0	1.0	0.0	0.0	0.0	0.0	0.0

The probability density function (PDF) for the generalized extreme value distribution is stated as [39]

$$f(x|k,\mu,\sigma) = \left(\frac{1}{\sigma}\right)\exp\left[-\left(1+k\frac{(x-\mu)}{\sigma}\right)^{-\frac{1}{k}}\right]\left(1+k\frac{(x-\mu)}{\sigma}\right)^{-1-\frac{1}{k}}, \quad k \neq 0 \tag{5}$$

for

$$1 + k\frac{(x-\mu)}{\sigma} > 0. \tag{6}$$

In the equations, μ, σ and k are the location, the scale and the shape parameters. For $k = 0$ the PDF has the form

$$f(x|0,\mu,\sigma) = \left(\frac{1}{\sigma}\right) \exp\left[-\exp\left(-\frac{(x-\mu)}{\sigma}\right) - \frac{(x-\mu)}{\sigma}\right]. \quad (7)$$

The PDF of the generalized Pareto distribution is expressed as a function of the shape parameter α, scale parameter β and the threshold parameter σ as [39]

$$f(x|\alpha,\beta,\gamma) = \left(\frac{1}{\beta}\right)\left[1+\alpha\frac{(x-\gamma)}{\beta}\right]^{-1-\frac{1}{\alpha}}, \quad \alpha \neq 0 \quad (8)$$

for $\gamma < x$, when $\alpha > 0$ or for $\gamma < x < -\beta/\alpha$ when $\alpha < 0$. For $\alpha = 0$ the PDF is

$$f(x|0,\beta,\gamma) = \left(\frac{1}{\beta}\right) \exp -\frac{(x-\gamma)}{\beta} \quad (9)$$

for $\gamma < x$.

The distribution parameters for the dipole and double loop is gathered in Table 5. The suggested distributions differ from the ones usually seen in the literature, where S is often modeled as a log-normally [11, 36] or a normally [14] distributed variable.

Table 5. Path loss distributions and their parameters.

	TT	TH	TL	HL	LL	HH
Dipole	G	G	F	F	G	G
	$\alpha = -0.78$	$\alpha = -0.75$	$k = -0.13$	$k = -0.57$	$\alpha = -1.34$	$\alpha = -0.93$
	$\beta = 37.29$	$\beta = 14.84$	$\sigma = 9.43$	$\sigma = 5.08$	$\beta = 20.55$	$\beta = 6.97$
	$\gamma = -21.79$	$\gamma = -8.61$	$\mu = -4.44$	$\mu = -0.98$	$\gamma = -8.91$	$\gamma = -3.50$
Double loop	G	G	G	F	F	G
	$\alpha = -0.95$	$\alpha = -0.89$	$\alpha = -0.71$	$k = -0.57$	$k = -0.16$	$\alpha = -1.30$
	$\beta = 47.82$	$\beta = 29.15$	$\beta = 26.96$	$\sigma = 4.65$	$\sigma = 5.48$	$\beta = 19.06$
	$\gamma = -27.07$	$\gamma = -14.94$	$\gamma = -15.17$	$\mu = -0.89$	$\mu = -2.43$	$\gamma = -9.18$

4.4. Statistical Amplitude Models

The statistical distributions of the absolute values of the CIR amplitudes are solved for each CIR tap separately. This means, that the fitting is performed on the linear amplitude values obtained from the VNA corresponding to the scattering parameter S_{21}. The number of CIR taps under examination is based on [4] which defines the sensitivity of the UWB receiver to be at minimum -91 dBm. The noise figure is assumed to be 10 dB and implementation losses 5 dB. The Federal Communications Commission (FCC) limits the maximum transmit power to be -41.3 dBm/MHz in the 3.1–10.6 GHz band corresponding to -14.3 dBm at a bandwidth of 499.2 MHz [3]. Assuming a safety margin of 5 dB, it can be concluded that the maximum path loss that needs to be considered is 82 dB. The average path loss of the CIRs for each separate tap and category are shown in Figs. 6(a) and 6(b). The threshold value of 82 dB is expressed as the horizontal line without markers. As a result, considered CIR tap numbers lie between 3–36 depending on the category and antenna type, as listed in Table 6. Considering the viewpoint of practicality when used in simulations and possible implementation in RAKE-type receivers, the maximum considered CIR tap number was limited to be 12. The utilization of longer delays would not offer considerable increase in the received energy. The maximum considered taps are lower for the dipole than the double loop in all cases except the LL. The CIRs seem to decay slightly faster for the dipole in the other five classes. This was noticed also in [19] which used the same antennas and antenna locations in extracting the generic statistical channel model.

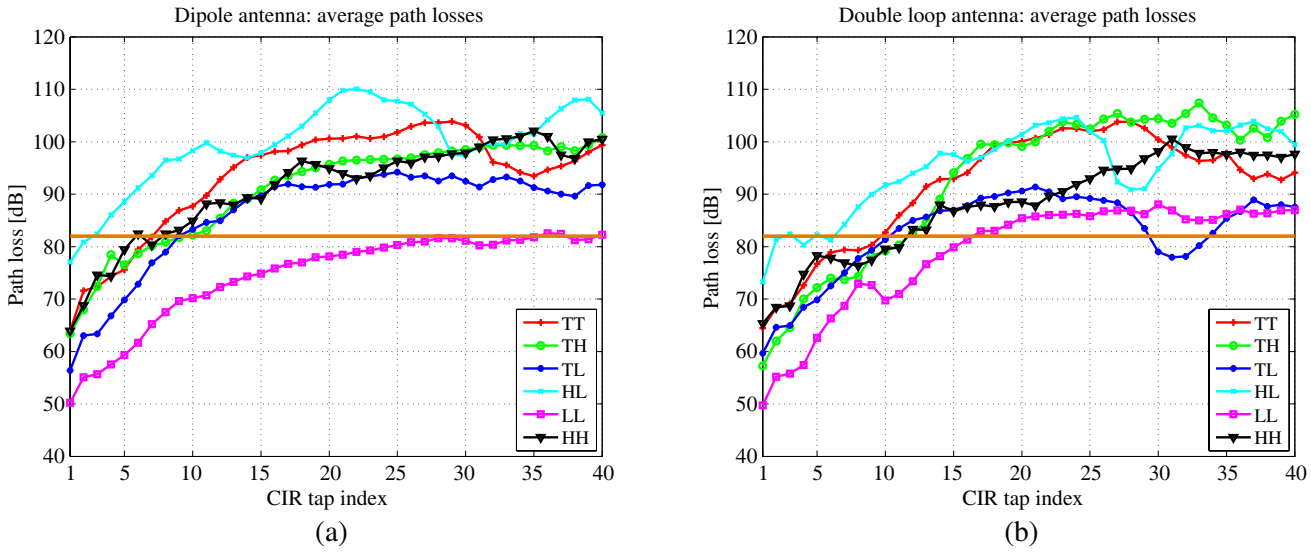

Figure 6. Average CIR path loss for individual taps. (a) Dipole. (b) Double loop.

Table 6. CIR tap numbers exceeding the threshold.

	TT	TH	TL	HL	LL	HH
Dipole	7	9	9	3	36 (12)	6
Double loop	10	12	11	3	17 (12)	12

The data were fitted against the same distribution selection as in Section 4.3 using the AICc criterion. The Δ_i reached values between the orders 10^2–10^4 and $w_i = 1$ for the best fit. To save space, these values are not listed. The best fit in all cases was noted to be the inverse Gaussian distribution that follows the PDF [39]

$$f(x|\rho,\phi) = \sqrt{\frac{\phi}{2\pi x^3}} \exp\left[-\frac{\phi}{2\rho^2 x}(x-\rho)^2\right], \quad x > 0, \tag{10}$$

where $\rho > 0$ and $\phi > 0$ are the mean and shape parameters, respectively.

The numerical values of the obtained distribution models are collected in Table 7 for the dipole antenna and in Table 8 for the double loop antenna.

Usually the suitable distributions reported to model static on-body UWB CIRs are the log-normal [7, 13, 15] or Weibull distributions [7, 15]. The inverse Gaussian distribution is not as commonly referred but was found to be the best model in the earlier articles of the authors in [19] for the double loop antenna and in [23] for both antennas. It should be noted though that differences exist between these references when comparing the distribution selection, antennas and measurement setup. Also the distribution ranking criterion is not in all references similar to the one applied in this article.

Figure 7 shows as an example the empirical and modeled CIRs and PDFs of TL category with the double loop antenna. The modeled values are obtained by producing CIRs extracted from the inverse Gaussian distribution with the parameters presented in Table 8. The number of iterations is similar to the number of empirical CIRs available, i.e., 9200. In Fig. 7(a) both the empirical and modeled averaged CIRs are visible. Also all empirical CIRs sweep by sweep are shown. The average empirical and modeled CIR graphs follow each others almost perfectly. Fig. 7(b) shows empirical and modeled PDFs for the first (upper figure) and fourth (lower figure) CIR tap. Differences clearly exist between the PDFs of the empirical and modeled data. On the average the model is quite accurate based on the average CIRs in Fig. 7(a) and is the best model of the tested 17 single distribution based on the AICc. However, as a future work it would be interesting to examine more complex distributions such

Table 7. Statistical amplitude parameters for the dipole antenna.

		CIR tap number of the dipole case											
		1	2	3	4	5	6	7	8	9	10	11	12
		Values must be multiplied by $\cdot 10^{-5}$											
TT	ρ	63.49	26.39	24.07	19.24	16.58	10.66	8.10	-	-	-	-	-
	ϕ	8.40	4.32	2.43	1.70	2.55	1.54	1.86	-	-	-	-	-
TH	ρ	67.61	39.91	24.03	11.99	14.94	11.68	9.84	9.05	8.20	-	-	-
	ϕ	86.79	42.70	33.80	17.97	14.66	9.42	10.75	11.00	12.03	-	-	-
TL	ρ	152.17	70.71	67.87	45.66	32.14	22.78	14.30	11.31	7.91	-	-	-
	ϕ	26.25	9.93	13.17	16.30	12.43	10.73	6.82	4.07	3.67	-	-	-
HL	ρ	14.11	9.08	7.54	-	-	-	-	-	-	-	-	-
	ϕ	33.50	3.21	4.01	-	-	-	-	-	-	-	-	-
LL	ρ	307.90	176.62	164.73	133.24	108.39	82.49	54.77	42.16	32.97	31.03	29.06	24.35
	ϕ	396.92	153.17	132.08	77.64	22.78	26.98	22.33	15.10	9.00	5.29	3.92	5.00
HH	ρ	63.84	36.61	18.71	19.17	10.67	7.57	-	-	-	-	-	-
	ϕ	121.30	51.85	63.74	72.09	92.08	7.12	-	-	-	-	-	-

Table 8. Statistical amplitude parameters for the double loop antenna.

		CIR tap number of the double loop case											
		1	2	3	4	5	6	7	8	9	10	11	12
		Values must be multiplied by $\cdot 10^{-5}$											
TT	ρ	60.05	38.44	35.26	23.34	14.65	11.38	10.74	10.81	9.65	7.32	–	–
	ϕ	4.52	1.51	2.30	2.47	1.22	1.37	1.48	1.34	0.96	0.74	-	-
TH	ρ	137.31	79.59	59.28	31.55	24.54	20.05	20.65	19.29	12.33	11.01	9.66	7.37
	ϕ	55.87	32.76	25.76	14.66	35.67	16.89	36.77	17.48	13.34	18.33	14.70	5.85
TL	ρ	104.02	58.81	56.53	37.86	32.17	23.69	17.75	12.96	10.81	8.55	6.72	-
	ϕ	19.63	6.83	14.71	11.85	6.67	8.67	8.16	8.35	4.21	3.72	2.59	-
HL	ρ	21.69	8.55	7.59	-	-	-	-	-	-	-	-	-
	ϕ	58.84	16.61	12.23	-	-	-	-	-	-	-	-	-
LL	ρ	326.97	174.65	162.23	134.93	74.45	48.56	36.73	22.62	23.30	32.65	28.32	21.48
	ϕ	195.77	73.57	29.63	25.54	15.78	13.27	9.95	10.48	7.59	4.78	6.09	5.14
HH	ρ	54.08	37.83	36.82	18.36	12.16	12.86	14.29	15.25	13.44	10.52	10.20	6.83
	ϕ	83.40	52.65	43.97	13.28	21.83	22.68	33.48	10.81	5.90	7.37	15.49	24.55

as the PDF model for shadowed conditions proposed in [40] or mixture models [38] consisting of a sum of several distributions.

4.5. CIR Delay Models

The CIR characteristics in the delay domain are reported in Table 9. At first, all indexes of all CIRs exceeding the 82 dB threshold were selected for the examination. The mean values of the CIR tap indexes (mean tap) lie between 2.3–29.2, median value (median tap) is within 2–26. In [19], values of 21.5 and 18.6 for the mean tap value were reported for the dipole and double loop cases, respectively. The median value was 10 for both antennas. In [19] the values were reported with an assumption that the first tap index is zero. The values are adjusted to correspond to this paper with an assumption that the index of the first CIR tap is one.

The highest CIR index describes the maximum observed value of the total excess delay (Max.

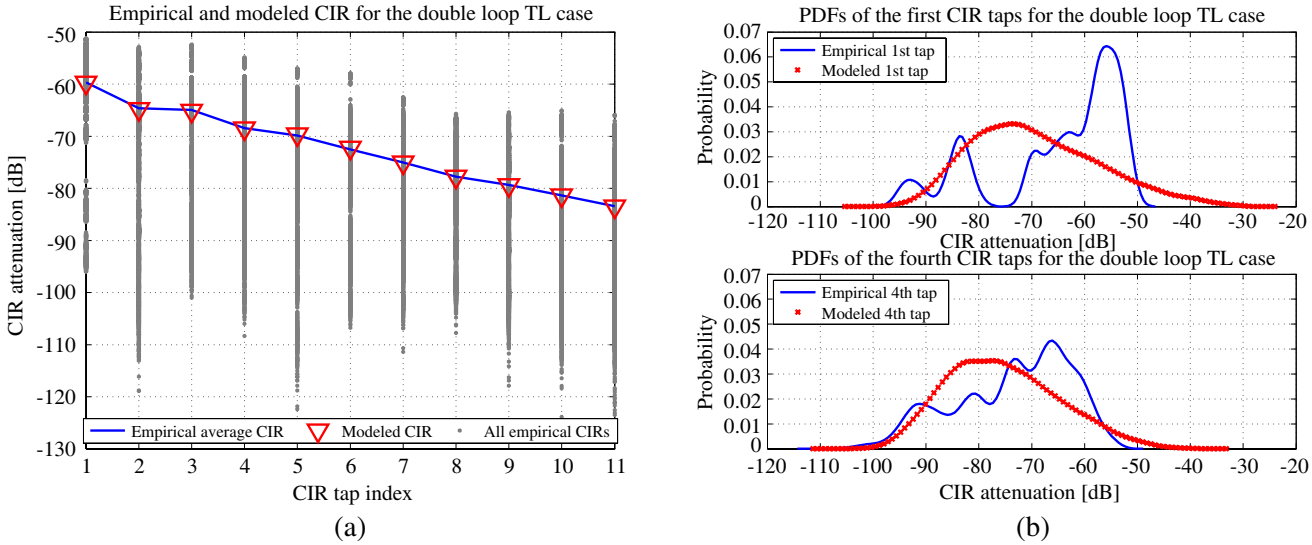

Figure 7. Example CIRs and PDFs for the double loop TL case. (a) Empirical and modeled CIRs. (b) Empirical and modeled PDFs.

TED) [41]. Max. TEDs are reported as well, although their large values are mainly due to the unideality of the anechoic chamber. The mean TED lies between 3.2–47.4 and the median TED between 3–41. The differences between the visual and numerical views between Fig. 6 and Table 9 is explained by noting that Fig. 6 shows averaged CIRs but Table 9 lists the values calculated from all separate VNA sweeps in the measured data. The indexes not exceeding the threshold are not included in the calculation in Table 9 but they have an effect on the average CIRs in Fig. 6.

The mean delay τ_0 corresponds the center gravity of the CIRs. It is calculated according to the equation [41]

$$\tau_0 = \frac{1}{P_T} \sum_{i=1}^{n} P_i \tau_i, \tag{11}$$

where P_i and τ_i are the power and delay in the CIR tap i and P_T is the total power of the CIR defined as

$$P_T = \sum_{i=1}^{n} P_i. \tag{12}$$

The values for τ_0 range between 1.8–12.4 taps. The values in Table 9 can be transferred into time scale by multiplying them with the time resolution $\Delta t \approx 0.167$ ns.

Another common channel parameter in the root-mean-square (RMS) delay spread that takes into account the delays and relative powers of the CIR taps. It is defined by the equation [41]

$$\tau_{\mathrm{RMS}} = \sqrt{\frac{1}{P_T} \sum_{i=1}^{n} P_i \tau_i^2 - \tau_0^2}. \tag{13}$$

The values for RMS delay spread vary between $\tau_{\mathrm{RMS}} = 1.5$–14.4 taps. The mean delay and RMS delay spread show slightly higher values for the double loop compared to the dipole antenna.

The link dependability (LD) in per cents expresses the amount of such separate VNA sweeps where at least one CIR tap exceeds the threshold. Links with CIRs not exceeding the threshold are considered to be unsuitable for communication. In seven cases out of twelve the LD is 100%. The most unreliable is the TT category that has LD values of 81.5% and 59.5% for the dipole and double loop, respectively. TL has LD of approx. 94% for both antennas. HL has a LD of 74% for the dipole but for the double loop case the LD is 100%. The high difference in HL is most likely due to the variations in limb positions and antenna installations causing a high shadowing in some measurement.

Table 9. CIR delay parameters.

		TT	TH	TL	HL	LL	HH
Dipole	Mean tap	15.2	5.5	15.6	2.3	29.2	5.2
	Median tap	5	5	7	2	26	4
	Max. TED	84	13	98	31	96	38
	Mean TED	19.5	7.6	27.3	3.2	47.4	9.9
	Median TED	8	7.5	15	3	41	8
	τ_0	7.3	2.4	5.1	1.8	2.7	2.1
	τ_{RMS}	8.6	2.8	7.1	1.5	4.4	2.7
	LD [%]	81.5	100.0	93.9	74.0	100.0	100.0
	TD: r	0.6714	3.7155	0.8823	9.1832	1.4279	2.7264
	TD: p	0.0422	0.4045	0.0536	0.7973	0.0465	0.3448
	TEDD: r	0.7766	5.3321	1.3788	5.0740	2.0517	4.4384
	TEDD: p	0.0383	0.4124	0.0480	0.6099	0.0415	0.3095
Double loop	Mean tap	15.6	9.8	20.5	16.8	19.5	7.0
	Median tap	6	6	9	6	14	7
	Max. TED	82	69	103	57	80	38
	Mean TED	20.9	16.4	35.1	24.5	38.7	13.0
	Median TED	9	11	32	28	45	12
	τ_0	7.2	2.8	7.8	12.4	5.6	3.2
	τ_{RMS}	8.2	4.2	10.1	14.4	8.2	4.1
	LD [%]	59.5	100.0	93.7	100.0	100.0	100.0
	TD: r	0.7986	1.0806	0.9425	0.7321	1.3721	2.9779
	TD: p	0.0486	0.0991	0.0440	0.0418	0.0657	0.2982
	TEDD: r	1.3089	1.2074	1.5542	1.1567	2.4199	6.5140
	TEDD: p	0.0590	0.0685	0.0424	0.0451	0.0588	0.3338

For the statistical delay models, firstly the indexes of all CIR taps exceeding the PL threshold (TD) were fitted for both antennas with the discrete binomial, negative binomial and Poisson distributions. They were ranked with the AICc criterion. The values of Δ_i and w_i are not listed to save space. Secondly, the distributions of the total excess delays (TEDDs) were solved with the similar method. The negative binomial distribution ended up to be the most suitable distribution in all cases with the discrete PDF, i.e., the probability mass function (PMF) [39]

$$f(x|r,p) = \begin{cases} \binom{r+x+1}{x} p^r (1-p)^x, & r \in \{0,1,2,\ldots\} \\ \dfrac{\Gamma(r+x)}{\Gamma(r)\Gamma(x+1)} p^r (1-p)^x, & r \in R_{>0} - N_{>0}, \end{cases} \tag{14}$$

where r and $0 < p \leq 1$ are the parameters of the distribution. If r is an integer $\in \{0,1,2,\ldots\}$, the upper equation is valid but for non-integer positive values ($r \in R_{>0} - N_{>0}$) the lower one should be applied, where Γ denotes for the gamma function [39]

$$\Gamma(x) = \int_0^\infty e^{-t} t^{x-1} dt. \tag{15}$$

The parameters to model the distributions of TD and TEDD cases are listed in the Table 9. Fig. 8(a) shows as an example the empirical and modeled PMF of the TD case for the double loop. Fig. 8(b) shows the corresponding example PMFs for the TEDD case. The modeled curves follow relatively well

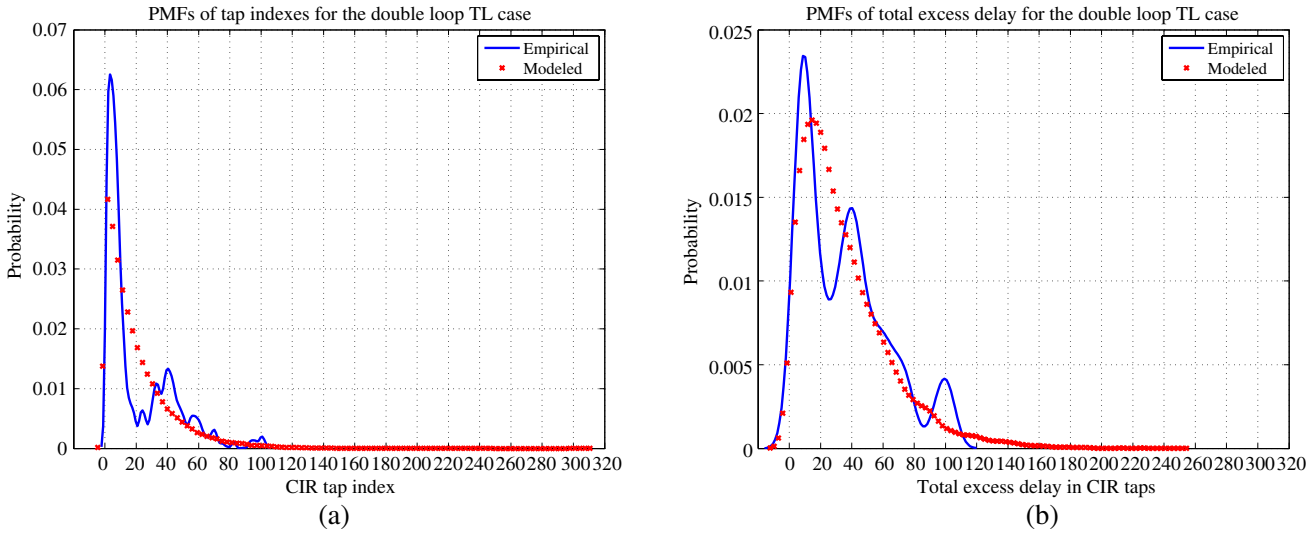

Figure 8. Example PMFs for the double loop TL case. (a) PMFs of the empirical and modeled tap indexes. (b) PMFs of the empirical and modeled total excess delays.

the empirical data. As mentioned with statistical amplitude modeling in Section 4.4, the usage of, e.g., multi-distribution models would be an interesting work in the future.

5. CONCLUSIONS AND FUTURE WORK

This article discusses on categorized on-body UWB channel modeling. The presented work is based on frequency domain measurements at 2–8 GHz frequency band in an anechoic chamber using a vector network analyzer. For the purposes of the analysis the IFFT was applied to obtained data to extract the time domain CIRs. Fourteen locations were selected on a human body reflecting the existing or easily assumed positions for sensors measuring the functions in the body. Two different prototype antennas were used: the dipole and double loop antenna and the measurements were conducted for both antennas. Four antennas were attached on the body at a time and the antenna separation from the body was kept constant at 20 mm.

Several references on the topic are working on a generic case where the on-body radio channels are examined without dividing them in any way. If a difference between the links is made, it is usually based on separating the cases of LOS, OLOS/QLOS or NLOS cases. The presented approach in this article is about categorizing the links with an objective method based on the antenna on-body locations. As a result, six categories are obtained: torso-torso, torso-head, torso-limb, head-limb, limb-limb and head-head. The path loss models are noted to vary heavily depending on the link category under examination. The path loss exponent show values between $n = 2.5$–7.5. The average PLs have values $\overline{X}_{\mathrm{PL}} = 49.7$–$77.0$ dB depending on the link category and the antenna type. The best link type with the lowest path loss is the limb-limb, the poorest one is the head-limb. The body shadowing appears to be the dominant factor in many cases. This leads, e.g., to the conclusion that the classical approach to model the path loss as a function of distance is not always suitable in on-body WBAN cases. In short links, the obstructing objects are often very close to the transmitter and/or receiver end of the links. As a result, the effect of the distance on the path loss will be buried in the effects caused by the shadowing.

The distribution of the shadowing term in the path loss model is found to follow either the generalized Pareto or generalized extreme value which is a different result from the ones usually reported in the references. The distributions were ranked according to the AICc. The CIR lengths worth considering in the receiver are 3–36 taps, calculated from the averaged CIRs. Head-limb links have the shortest response and limb-limb links the longest ones. Considering the viewpoint of practicality, the number of CIR taps in the statistical amplitude models was limited to 12. The amplitude distribution of

the CIRs is modeled best with a the inverse Gaussian distribution which also differs from the typically seen results.

The CIR tap numbers exceeding the threshold was analyzed to give a view on the behavior of the delay spread. Mean tap number has a value between 2.3–29.2 and the median value 2–26. The mean and median values of the total excess delays are between 3.2–47.4 and 3–41 taps, respectively. The mean delay has values $\tau_0 = 1.8$–12.4 taps and the RMS delay spread $\tau_{\mathrm{RMS}} = 1.5$–$14.4$ taps. The link dependability is lowest with the TT links. For the other categories, the link dependability is generally speaking high. The distribution of the indexes of the CIR taps exceeding the threshold is described best with the negative binomial distribution. Also the distributions of the CIR total excess delays are modeled with the same distribution.

Comparison between antennas does not show very clear differences. The CIRs appear to decay faster in most cases for the dipole antenna. The statistical characteristics of the channels can be modeled with the same distributions for both antennas.

In the future, the measurements will be extended in echoic environments as well as in dynamic cases. The suitability of more complex distribution models should be tested and their effect of different models on the true, e.g., bit error rate of a system would be interesting to see compared to the single distribution models.

ACKNOWLEDGMENT

The work has been partly funded by the Finnish Funding Agency for Innovation (Tekes) by the project Wireless Body Area Network for Health and Medical Care (WiBAN-HAM).

REFERENCES

1. Hall, P. S. and Y. Hao, *Antennas and Propagation for Body-centric Wireless Communications*, Artech House, Norwood, 2012.
2. Hämäläinen, M., A. Taparugssanagorn, R. Tesi, and J. Iinatti, "Wireless medical communications using UWB," *Proc. IEEE Int. Conf. on Ultra-Wideband (ICUWB)*, 485–489, 2009.
3. Oppermann, I., M. Hämäläinen, and J. Iinatti, *UWB Theory and Applications*, John Wiley & Sons, West Sussex, 2004.
4. IEEE Standard for Local and Metropolitan Area Networks, IEEE 802.15.6-2012, Part 15.6: Wireless Body Area Networks, 2012.
5. Khan, M. M., Q. H. Abbasi, S. Liaqat, and A. Alomainy, "Comparison of two measurement techniques for UWB off-body radio channel characterisation," *Progress In Electromagnetics Research M*, Vol. 27, 179–189, 2012.
6. Garcia-Serna, R.-G., C. Garcia-Pardo, and J. Molina-Garcia-Pardo, "Effect of the receiver attachment position on ultrawideband off-body channels," *IEEE Antennas Wireless Propag. Lett.*, 1101–1104, 2015.
7. Taparugssanagorn, A., R. Tesi, C. Pomalaza-Ráez, M. Hämäläinen, and J. Iinatti, "Effect of body motion and the type of antenna on the measured UWB channel characteristics in medical applications of wireless body area networks," *Proc. IEEE Int. Conf. on Ultra-Wideband (ICUWB)*, 332–336, 2009.
8. Thotatewa, K. M. S., J.-M. Redoutè, and M. R. Yuce, "Propagation, power absorption and analysis of UWB wireless capsule endoscopy devices operating in the human body," *IEEE Trans. Microw. Theory Tech.*, Vol. 63, No. 11, 2015.
9. Mohammadi, Z., R. Saadane, and D. Aboutajdine, "New high-rate UWB scheme for WBAN-based healthcare systems," *Progress In Electromagnetics Research B*, Vol. 60, 125–139, 2014.
10. Abbasi, Q. H., M. H. Khan, S. Liaqat, M. Kamran, A. Alomainy, and Y. Hao, "Experimental investigation of ultra wideband diversity techniques for on-body radio communications," *Progress In Electromagnetics Research C*, Vol. 34, 165–181, 2013.

11. Gao, A.-M., Q.-H. Xu, H.-L. Peng, W. Jiang, and Y. Jiang, "Performance evaluation of UWB on-body communication under WiMAX off-body EMI existence," *Progress In Electromagnetics Research*, Vol. 132, 479–498, 2012.
12. Alomainy, A., Y. Hao, X. Hu, C. G. Parini, and P. S. Hall, "UWB on-body radio propagation and system modelling for wireless body-centric networks," *IEE Proc. Commun.*, Vol. 153, No. 1, 107–114, 2006.
13. Fort, A., C. Desset, P. de Doncker, P. Wambacq, and L. van Biesen, "An ultra-wideband body area propagation channel — From statistics to implementation," *IEEE Trans. Microw. Theory Tech.*, Vol. 54, No. 4, 1820–1826, 2006.
14. Molisch, A. F., D. Cassioli, C.-C. Chong, S. Emami, A. Fort, B. Kannan, J. Karedal, J. Kunisch, H. G. Schantz, K. Siwiak, and M. Z. Win, "A comprehensive standardized model for ultrawideband propagation channels," *IEEE Trans. Antennas Propag.*, Vol. 54, No. 11, 3151–3166, 2006.
15. Di Bari, R., Q. H. Abbasi, A. Alomainy, and Y. Hao, "An advanced UWB channel model for body-centric wireless networks," *Progress In Electromagnetics Research*, Vol. 136, 79–99, 2013.
16. Alomainy, A., Y. Hao, C. G. Parini, and P. S. Hall, "Comparison between two different antennas for UWB on-body propagation measurements," *IEEE Antennas Wireless Propag. Letters*, Vol. 4, 31–34, 2005.
17. Khaleghi, A. and I. Balasingham, "Non-line-of-sight on-body ultra wideband (1–6 GHz) channel characterisation using different antenna polarisations," *IET Microw. Antennas Propag.*, Vol. 3, No. 7, 1019–1027, 2009.
18. Kumpuniemi, T., T. Tuovinen, M. Hämäläinen, K. Yekeh Yazdandoost, R. Vuohtoniemi, and J. Iinatti, "Measurement-based on-body path loss modelling for UWB WBAN communications," *Proc. 7th Int. Symp. on Medical Inform. and Commun. Technology (ISMICT)*, 233–237, 2013.
19. Kumpuniemi, T., M. Hämäläinen, T. Tuovinen, K. Yekeh Yazdandoost, and J. Iinatti, "Generic small scale channel model for on-body UWB WBAN communications," *Proc. 2nd Ultra Wideband for Body Area Networking Workshop (UWBAN), Co-located with the 8th Int. Conf. on Body Area Networks (BodyNets)*, 570–574, 2013.
20. Vorobyov, A. V. and A. G. Yarovoy, "Human body impact on UWB antenna radiation," *Progress In Electromagnetics Research M*, Vol. 22, 259–269, 2012.
21. Wang, Q., T. Tayamachi, I. Kimura, and J. Wang, "An on-body channel model for UWB body area communications for various postures," *IEEE Trans. Antennas Propag.*, Vol. 57, No. 4, 991–998, 2009.
22. Klemm, M. and G. Troester, "EM energy absorption in the human body tissues due to UWB antennas," *Progress In Electromagnetics Research*, Vol. 62, 261–280, 2006.
23. Kumpuniemi, T., M. Hämäläinen, K. Yekeh Yazdandoost, and J. Iinatti, "Radio channel modelling for pseudo-dynamic WBAN on-body links," *Proc. 8th Int. Symp. on Medical Inform. and Commun.Technology (ISMICT)*, 1–5, 2014.
24. Oliveira, C., M. Mackowiak, and L. M. Correia, "Correlation analysis in on-body communications," *Proc. 9th European Conf. on Antennas and Propagation (EUCAP)*, 3383–3387, 2012.
25. Ali, K., A. Brizzi, S. L. Lee, G. Z. Yang, A. Alomainy, and Y. Hao, "Quantitative analysis of the subject-specific on-body propagation channel based on statistically created models," *IEEE Antennas Wireless Propag. Letters*, Vol. 14, 398–401, 2015.
26. Kumpuniemi, T., M. Hämäläinen, K. Yekeh Yazdandoost, R. Vuohtoniemi, and J. Iinatti, "Measurements for body-to-body UWB WBAN radio channels," *Proc. 9th European Conf. on Antennas and Propagation (EUCAP)*, 1–5, 2015.
27. Tuovinen, T., T. Kumpuniemi, K. Yekeh Yazdandoost, M. Hämäläinen, and J. Iinatti, "Effect of the antenna-human body distance on the antenna matching in UWB WBAN applications," *Proc. 7th Int. Symp. on Medical Inform. and Commun. Technology (ISMICT)*, 193–197, 2013.
28. Tuovinen, T., T. Kumpuniemi, M. Hämäläinen, K. Yekeh Yazdandoost, and J. Iinatti, "Effect of the antenna-body distance on the on-ext and on-on channel link path gain in UWB WBAN applications," *Proc. 35th Annu. Int. Conf. IEEE Eng. in Medicine and Biology Society (EMBC)*, 1242–1245, 2013.

29. Anliker, U., J. A. Ward, P. Lukowicz, G. Troster, F. Dolveck, M. Baer, F. Keita, E. B. Schenker, F. Catarsi, L. Coluccini, A. Belardinelli, D. Shklarski, M. Alon, E. Hirt, R. Schmid, and M. Vuskovic, "AMON: A wearable multiparameter medical monitoring and alert system," *IEEE Trans. on Inf. Technol. Biomed.*, 415–427, 2004.
30. Penders, J., J. van de Molengraft, L. Brown, B. Grundlehner, B. Gyselinckx, and C. van Hoof, "Potential and challenges of body area networks for personal health," *Proc. 31st Annu. Int. Conf. IEEE Eng. in Medicine and Biology Society (EMBC)*, 6569–6572, 2009.
31. Zheng, Y.-L., X.-R. Ding, C. C. Y. Poon, B. P. L. Lo, H. Zhang, X.-L. Zhou, G.-Z. Yang, N. Zhao, and Y.-T. Zhang, "Unobtrusive sensing and wearable devices for health informatics," *IEEE Trans. Biomed. Eng.*, Vol. 61, No. 5, 1538–1554, 2014.
32. Keränen, N., M. Särestöniemi, J. Partanen, M. Hämäläinen, J. Reponen, T. Seppänen, J. Iinatti, and T. Jämsä, "IEEE802.15.6-based multi-accelerometer WBAN system for monitoring Parkinson's disease," *Proc. 35th Annu. Int. Conf. IEEE Eng. in Medicine and Biology Society (EMBC)*, 1659–1659, 2013.
33. Demonceau, M., A.-F. Donneau, J.-L. Croisier, E. Skawiniak, M. Boutaayamou, D. Maquet, and G. Garraux, "Contribution of a trunk accelometer system to the characterization of gait in patients with mild-to-moderate Parkinson's disease," *IEEE J. Biomed. Health Inform.*, Vol. 19, No. 6, 1803–1808, 2015.
34. Jakob, C., P. Kugler, F. Hebenstreit, S. Reinfelder, U. Jensen, D. Schuldhaus, M. Lochmann, and B. M. Eskofier, "Estimation of the knee flexion-extension angle during dynamic sport motions using body-worn inertial sensors," *Proc. 8th Int. Conf. on Body Area Networks (BodyNets)*, 289–295, 2013.
35. Devore, J. and R. Peck, *Statistics, The Exploration and Analysis of Data*, Wadsworth Publishing Company, Belmont, 1993.
36. Wang, J. and Q. Wang, *Body Area Communications — Channel Modeling, Communication Systems and EMC*, John Wiley & Sons, Singapore, 2013.
37. Smith, D. B., D. Miniutti, T. A. Lamahewa, and L. W. Hanlen, "Propagation models for body-area networks: A survey and new outlook," *IEEE Antennas Propagat. Mag.*, Vol. 55, No. 5, 97–117, 2013.
38. Burnham, K. P. and D. R. Anderson, *Model Selection and Multimodel Inference, A Practical Information — Theoretic Approach*, 2nd Edition, Springer-Verlag, New York, 2002.
39. Mathworks, MATLAB, Documentation Center, Statistics Toolbox, (accessed in November 2015). [Online] available: http://se.mathworks.com/help/stats/index.html.
40. Cotton, S. L., "A statistical model for shadowed body-centric communications channels: Theory and validation," *IEEE Trans. Antennas Propag.*, Vol. 62, No. 3, 1416–1424, 2014.
41. Saunders, S. R. and A. Aragón-Zavala, *Antennas and Propagation for Wireless Communication Systems*, 2nd Edition, John Wiley & Sons, West Sussex, 2007.